We are IntechOpen,
the world's leading publisher of
Open Access books
Built by scientists, for scientists

4,800
Open access books available

122,000
International authors and editors

135M
Downloads

Our authors are among the

154
Countries delivered to

TOP 1%
most cited scientists

12.2%
Contributors from top 500 universities

CLARIVATE ANALYTICS
BOOK CITATION INDEX
INDEXED

WEB OF SCIENCE™

Selection of our books indexed in the Book Citation Index
in Web of Science™ Core Collection (BKCI)

Interested in publishing with us?
Contact book.department@intechopen.com

Numbers displayed above are based on latest data collected.
For more information visit www.intechopen.com

Optical Properties and Electronic Band Structures of Perovskite-Type Ferroelectric and Conductive Metallic Oxide Films

Zhigao Hu[1], Yawei Li[1], Wenwu Li[1], Jiajun Zhu[1],
Min Zhu[2], Ziqiang Zhu[3] and Junhao Chu[3]
[1]*Key Laboratory of Polar Materials and Devices, Ministry of Education,*
Department of Electronic Engineering, East China Normal University, Shanghai 200241
[2]*Department of Physics, Shanghai Jiao Tong University, Shanghai 200240*
[3]*Key Laboratory of Polar Materials and Devices, Ministry of Education,*
Department of Electronic Engineering, East China Normal University, Shanghai 200241
People's Republic of China

1. Introduction

Ferroelectric (FE) materials have recently attracted considerable attention and intensive research due to their unique advantages in nonvolatile random-access memories, electro-optic devices, pyroelectric detectors, and optical mixers. (1; 2; 3; 4; 5; 6) It is well known that FE films can be deposited directly on diversified substrates and are expected to yield better sensitivity and faster response than the equivalent bulk single crystal. Nevertheless, the physical properties of FE films are strongly sensitive to the experimental conditions containing substrate, growth technique, crystalline quality, intrinsic defects, and doping elements, etc. Hence, it is significant to systematically investigate the physical properties of FE film materials, such as optical, electrical, and magnetic properties and their interactions. Among them, perovskite-type FE materials are the most promising compounds due to the polarization from the oxygen octahedra. Although there are lots of electrical properties reported on the FE bulk and film materials, optical and electronic properties are still scarce for their applications in the optoelectronic field. As we know, $Bi_4Ti_3O_{12}$ (BiT) is a very promising compound as a candidate of FE materials for integrated optics applications due to their combination of low processing temperatures, fatigue-free properties, high Curie temperature ($T_c \sim 675$ °C) and large spontaneous polarization ($P_s \sim 50$ $\mu C/cm^2$ along the a axis). (7; 8) Moreover, it was reported that the FE and optical properties of BiT materials can be evidently improved by the La doping, such as $Bi_{3.25}La_{0.75}Ti_3O_{12}$ (BLT). (9; 10; 11; 12) For Bi-site substitution, the coercive field usually becomes larger than that of pure BiT, while for Ti-site substitution, the coercive field becomes smaller. Theoretical calculation indicates that the La substitution strikingly decreases the T_c to about 400 °C. (13) Thus, BLT material can be widely accepted for an interesting compound in some optoelectronic applications owing to a lower T_c and larger coercive field.

Generally, the phase transitions of perovskite-based oxides represent a basilic class of structural phase transition that bear significant technological implications. (14) The high

FE phase transition temperature will be valuable for the electronic and optoelectronic device applications, which can be controlled at room temperature (RT). As we know, the phase transition of most FE materials can be derived by the soft mode, which can be studied by Raman scattering and/or far-infrared spectroscopy. (15; 16) Note that the ferroelectric-paraelectric phase transition of FE materials have been widely investigated to clarify the T_c with the aid of electrical measurements, such as the remnant polarization variations. However, there are some other structural transitions in FE materials except for the T_c temperature, which are also crucial to the polarization. (17; 18; 19) It can be expected that the physical properties of FE compounds, such as dielectric constants and loss tangent could be changed due to the structure variations at phase transition point. Therefore, the investigations on the optical properties during the phase transitions are necessary to further clarify its FE derivation and polarization.

For BiT nanocrystals and ceramics, some experimental results reveal a possible structural transformation at lower temperatures. (20; 21) Structural transitions are usually studied by various experimental techniques such as x-ray diffraction (XRD) and Raman scattering. (22; 23; 24) Although both of the two methods can provide the most direct information about the phase transitions, the variations of the optical band gap, optical constants, and band tail state behavior during phase transitions could not be derived due to the intrinsic technique limitations. Fortunately, far-infrared spectroscopy is commonly applied to observe the variation of soft mode and dielectric function during the phase transition. (15) Nevertheless, the band gap behavior and interband electronic transition are still keep as an open issue because of the wide-band-gap characteristics for most FE materials, which are located in the ultraviolet photon energy region. Therefore, current attention is focused on finding a new method to give more information about the phase transitions, especially for the band gap region. Motivated by the lack of experimental data about the dielectric functions and phase transitions for BLT film, here we focus on the optical properties of BLT nanocrystalline film with different temperatures to gain a more intensive understanding of the microscopic mechanism of phase transitions and novel physics in these materials.

On the other hand, top and bottom electrodes play an important role in optoelectronic devices in order to deal with electrical and/or optical signal. (25; 26; 27; 28; 29) For example, polarization charges, which can be screened by free carriers inside the electrode, are induced at the electrode/FE interface in a FE-based capacitor. As we know, $LaNiO_3$ (LNO) and $La_{0.5}Sr_{0.5}CoO_3$ (LSCO), which are the highly conductive metallic oxides, have a distorted perovskite structure with a cubic lattice parameter of 3.84 and 3.83 Å, respectively. (30; 31; 32) As the matched electrodes for perovskite FE-based devices, LNO and LSCO materials have been widely studied as alternatives for platinum (Pt) and Pt-based metals. (26; 29; 33) It is because these metallic oxides can significantly improve the physical properties of FE devices, as compared with noble metal electrodes. (33; 34) Therefore, understanding the intrinsic physical phenomena occurring within FE film and electrode/FE interface requires accurate knowledge of dielectric constants about the electrode. Owing to an increasing interest of nanostructured FE materials and devices, (35; 36) the physical properties of nanostructured electrodes should be further investigated in order to clarify the functionalities. In spite of the promising properties up to now, (27; 32; 29) there are no reports on dielectric function and optical conductivity of nanostructured LNO and LSCO materials, which can predicatively reflect the electrical transport properties and electronic band structure. (37; 38) It is well known that macroscopical dielectric function and/or optical conductivity can be directly related to the electronic band structure. (39) In particular, the optical and electronic properties

could be remarkably different from the bulk crystal for LNO and LSCO materials with a low-dimensional structure. (38) Therefore, it is necessary to clarify the optical response behaviors of the nanostructured oxides.

Fortunately, optical transmittance, reflectance, and spectroscopic ellipsometry techniques, which are the nondestructive and powerful technique to investigate the optical characteristics of materials, can directly provide electronic band energy and dielectric constants, etc. (40; 41; 42; 43) With the aid of the reasonable dielectric function model, one can reproduce the experimental spectra well and the dielectric functions can be easily extracted. (44) This makes it possible to investigate the optical properties of wide band gap FE films and conductive metallic oxide films in a wider photon energy range. In particular, Spectroscopic ellipsometry, which is very sensitive to ultrathin films and surfaces, is a nondestructive and powerful technique to investigate the optical characteristics of materials, and, in particular, to measure the thickness and the dielectric function of a multilayer system simultaneously. (44; 45; 46; 47; 48; 49) As compared to the traditional reflectance and/or transmittance spectroscopy, spectroscopic ellipsometry can determine exactly the ratio of linearly *p*- and *s*-polarized light intensity and the phase difference between *p*- and *s*-polarized light simultaneously. Therefore, spectroscopic ellipsometry can directly provide the optical constants of materials without Kramers-Krönig (K-K) analysis. (49; 50) The purpose of the present work is to point out that spectral technique is an effective tool to study the structural properties and phase transitions in FE materials and interband transitions in conductive metallic oxides. The results open a new vista for the experimental technique development of observing phase/structural transitions. Moreover, it indicates that the spectral techniques can be applied to study the optical response behavior of perovskite-type FE and conductive metallic oxides.

This chapter is arranged in the following way. In Sec. 2, the detailed growth processes of the BLT, LNO, and LSCO films and spectral setup are described; In Sec. 3, the crystal structures of the BLT, LNO and LSCO films have been presented; In Sec. 4, spectral transmittance, reflectance and ellipsometric theory is expressed; In Sec. 5, optical properties and phase transition characteristics of the BLT films have been discussed. In Sec. 6, the electronic band structures of the LNO and LSCO films on Si substrate are derived in detail; In Sec. 7, the thickness dependence of infrared optical constants in the LNO films on platinized silicon substrates (Pt/Ti/SiO$_2$/Si) is presented; In Sec. 8, the main results are summarized.

2. Experimental

2.1 The fabrications of BLT films

The BLT nanocrystalline film was prepared on quartz substrate by chemical solution deposition technique. Bismuth nitrate, lanthanum acetate, and titanium butoxide were used as starting materials. The BLT precursor solution with a stoichiometric molar ratio of Bi/La/Ti=3.25/0.75/3 was dissolved in heated glacial acetic acid instead of drastic toxicity 2-methoxyethanol, which makes the process of preparation of precursor solutions safer and simpler. Note that excess 8 mol% Bi precursor was added to compensate for Bi evaporation during the annealing process. Then an appropriate amount of acetylacetone was added to the solution as a stabilizing agent. Equimolar amounts of titanium butoxide were also added into solution. The concentration of the precursor solution was 0.05 M. In order to improve the hydrolysis and polymerization, the precursor solution was placed at atmosphere about 10 days before spin coating onto the substrate. The homogeneity and stability of the coating solution was greatly improved by the addition of acetylacetone. The BLT nanocrystalline film was deposited by spin coating of the solution onto quartz substrate at 3500 rpm for 30

s. Each layer was dried at 180 °C for 3 min, then calcined at 350 °C for 3 min. Finally, the samples were annealed at 675 °C for 3 min by rapid thermal annealing. By repeating the coating/calcining cycles about five times, the BLT film with the nominal thickness of about 150 nm can be obtained.

2.2 The growths of conductive metallic oxides

Nanocrystalline LNO and LSCO films were deposited on the single-side polished silicon (Si) wafers by radio frequency magnetron sputtering (RFMS) and pulsed laser deposition (PLD) methods, respectively. A 100-mm-diam LNO target was used for deposition. The distance between the target and Si(111) substrates was 70 mm. Before deposition, the target was pre-sputtered for 30 min with the substrate shutter closed to achieve stable conditions. The vacuum chamber pumped by a turbomolecular pump produced a base pressure of 2×10^{-4} Pa and was raised to 1.6 Pa by admitting argon (Ar) and oxygen (O_2). The Si(111) substrates were mounted with silver paste onto a resistively heated substrate holder. During the sputtering, the temperature of the substrate holder was kept at 265 °C and the radio frequency power on the target was 80 W, operating at 13.56 MHz, yielding a growth rate of about 2-3 nm/min. After deposition, a cooling was carried out in vacuum. Following with the above method, the LNO film with the nominal thickness of about 230 nm can be derived.

For the LSCO film, however, a KrF excimer laser with the pulse frequency of 5 Hz was used for the growth. The oxygen pressure was controlled at 25 Pa during the deposition process. The substrates were cleaned in pure ethanol with an ultrasonic bath to remove physisorbed organic molecules from the Si surfaces. Then the substrates were rinsed several times with de-ionized water. Finally the wafers were dried in a pure nitrogen stream before the deposition of the LSCO films. The ceramic LSCO target with a La:Sr stoichiometric ratio of 0.5:0.5 was sintered by solid state reaction. The substrate temperature was kept at 700 °C. In order to obtain the nominal thickness of about 1 μm, the LSCO layers have been deposited during the several periods.

On the other hand, the sol-gel technique is applied to fabricate the LNO with different thickness on platinized silicon (Pt/Ti/SiO$_2$/Si) substrates. Lanthanum nitrate [La(NO$_3$)$_3$] and nickel acetate [Ni(CH$_3$COO)$_2$•4H$_2$O] were used as the start materials, and acetic acid and water were used as the solvents. Nickel acetate was dissolved in acetic acid and equimolar amounts of lanthanum nitrate dissolve in distilled water held at RT, respectively. Then the two solutions were mixed together with constant stirring. The concentration of the precursor solution was adjusted to 0.3 M by adding or distilling some acetic and water. The LNO films were deposited spin coating of the 0.3 M solution at the speed of 4000 rpm for 30 s. Each layer of the films was dried at 160 °C for 5 min, then pyrolyzed at 400 °C for 6 min to remove residual organic compounds, following annealed at 650 °C for 3 min in air by a rapid thermal annealing (RTA) process. The aforementioned coating, pyrolyzing and annealing were repeated different times in order to obtain the LNO films with different thickness.

2.3 The crystalline and optical characterizations

The crystallinity of the BLT, LNO, and LSCO films at RT was examined by XRD using a Ni filtered Cu Kα radiation source (D/MAX-2550V, Rigaku Co.). In the XRD measurement a vertical goniometer (Model RINT2000) was used, and continuous scanning mode (θ-2θ) was selected with a scanning rate of 10°/min and interval of 0.02°. The temperature dependent ultraviolet transmittance spectra were measured by a double beam ultraviolet-infrared spectrophotometer (PerkinElmer UV/VIS Lambda 2S) at the photon energy range of 1.1-6.5 eV
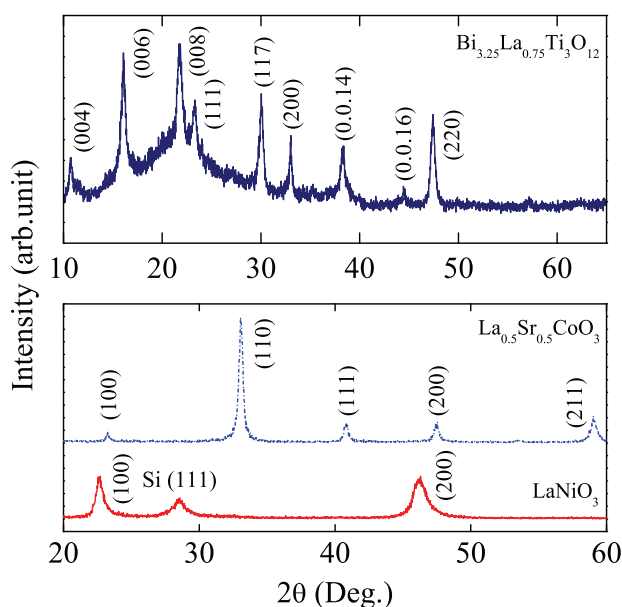
Fig. 1. The XRD patterns of $Bi_{3.25}La_{0.75}Ti_3O_{12}$, LNO and $La_{0.5}Sr_{0.5}CoO_3$ films, respectively.

(190-1100 nm). The BLT film was mounted into an optical cryostat (Optistat CF-V from Oxford Instruments) and the temperature was continuously varied from 80 to 480 K. Near-normal incident optical reflectance spectra ($\sim 8°$) were recorded at room temperature (RT) with a double beam ultraviolet-infrared spectrophotometer (PerkinElmer Lambda 950) at the photon energy from 0.47 to 6.5 eV (190-2650 nm) with a spectral resolution of 2 nm. Aluminum (Al) mirror, whose absolute reflectance was directly measured, was taken as reference for the spectra in the photon energy region. The ellipsometric measurements were carried out at RT by a variable-angle infrared spectroscopic ellipsoetry (IRSE) synchronously rotating polarizer and analyzer. The system operations, including data acquisition and reduction, preamplifier gain control, incident angle, wavelength setting and scanning were fully and automatically controlled by a computer. In this study, the incident angles were $70°$, $75°$ and $80°$ for the LNO films. Note that no mathematical smoothing has been performed for the experimental data.

3. The crystalline structures

Figure 1 (a) shows the XRD spectra of BLT, LNO, and LSCO nanocrystalline film. For the BLT film, there are the strong diffraction peaks (004), (006), (008), (117) and (220), which confirm that the present BLT nanocrystalline film has the tetragonal phase. Note that the broadening feature near $22°$ can be ascribed to the quartz substrate. On the other hand, the XRD patterns indicate that the LNO and LSCO films are crystallized with the single perovskite phase. It should be emphasized that the LNO film presents a highly (100)-preferential orientation. Besides the strongest (110) peak, some weaker peaks (100), (111), (200), and (211) appear, indicating that the LSCO film is polycrystalline. Generally, the grain size can be estimated by the well-known Scherrer's equation $r = K\lambda / \beta \cos\theta$, where r is the average grain size, β the full width at half maximum of the diffraction line, λ the x-ray wavelength, θ the Bragg angle, K the Scherrer's constant of the order of unity for usual crystals. For the BLT film on the quartz substrate, the average grain size from the (006) diffraction peak is estimated to about 16 nm. However, the grain size from the (200) and (110) peaks was evaluated to 78 and 27 nm for the LNO and LSCO films on Si substrates, respectively. Note that the grain size of the BLT and LSCO films is much less that that of the LNO film. The striking increment for the LNO film

could be due to the better crystallization (i.e., highly preferential orientation). It should be emphasized that the LNO films on the Pt/Ti/SiO$_2$/Si substrates are of the similar crystalline structure to that from the silicon substrate. Nevertheless, the grain size of the LNO films on the Pt/Ti/SiO$_2$/Si substrates is estimated to 18.4, 17.5 nm and 27.8 nm for the 100-nm, 131-nm and 177-nm thick films, respectively. It indicates that the average grain size is similar for the LNO films with the thickness of about 200 nm on different substrates.

4. Transmittance, reflectance and SE theory

4.1 Transmittance and reflectance

Generally, transmittance and reflectance spectra can be reproduced by a three-phase layered structure (air/film/substrate) for the film materials with a finite thickness. (40; 41; 42) For the BLT film, the three-phase layered structure configuration is applied due to the thickness of about 150 nm. Nevertheless, it is noted that the nominal growth thickness is about 230 nm and 1 μm for the LNO and LSCO films on Si substrates, respectively. Therefore, considering the light penetration depth in the films due to the optical conductivity, the three-phase layered model and the semi-infinite medium approach are applied to calculate the reflectance spectra of the LNO and LSCO films, respectively. (27; 51) The optical component of each layer is expressed by a 2×2 matrix. Suppose the dielectric function of the film is $\tilde{\varepsilon}$, vacuum is unity, and the substrate is $\tilde{\varepsilon}_s$, respectively. The resultant matrix M_r is described by the following product form

$$M_r = M_{vf} M_f M_{fs}. \tag{1}$$

Here, the interface matrix between vacuum and film has the form

$$M_{vf} = \frac{1}{2\sqrt{\tilde{\varepsilon}}} \left[\begin{array}{cc} (\sqrt{\tilde{\varepsilon}}+1) & (\sqrt{\tilde{\varepsilon}}-1) \\ (\sqrt{\tilde{\varepsilon}}-1) & (\sqrt{\tilde{\varepsilon}}+1) \end{array} \right]. \tag{2}$$

and the propagation matrix for the film with thickness is described by the equation

$$M_f = \left[\begin{array}{cc} \exp(i2\pi\sqrt{\tilde{\varepsilon}}d/\lambda) & 0 \\ 0 & \exp(-i2\pi\sqrt{\tilde{\varepsilon}}d/\lambda) \end{array} \right]. \tag{3}$$

where λ is the incident wavelength, and correspondingly the interface matrix between film and substrate is

$$M_{fs} = \frac{1}{2\sqrt{\tilde{\varepsilon}_s}} \left[\begin{array}{cc} (\sqrt{\tilde{\varepsilon}_s}+\sqrt{\tilde{\varepsilon}}) & (\sqrt{\tilde{\varepsilon}_s}-\sqrt{\tilde{\varepsilon}}) \\ (\sqrt{\tilde{\varepsilon}_s}-\sqrt{\tilde{\varepsilon}}) & (\sqrt{\tilde{\varepsilon}_s}+\sqrt{\tilde{\varepsilon}}) \end{array} \right]. \tag{4}$$

thus, the transmittance T and reflectance R can be readily obtained from

$$T = \text{Real}(\sqrt{\tilde{\varepsilon}}) \left| \frac{1}{M_{r1,1}} \right|^2, \quad R = \left| \frac{M_{r1,0}}{M_{r1,1}} \right|^2. \tag{5}$$

The multi-reflections from substrate are not considered in Eq (5). It should be emphasized that the absorption from the substrate must be taken into account to calculate the transmittance of the film-substrate system. (44)

The physical expression of the real and imaginary parts of the dielectric functions for semiconductor and insulator materials has been reported by Adachi. (52) The Adachi's model dielectric function is based upon the one electron interband transition approach, and relies upon the parabolic band approximation assuming energy independent momentum matrix elements. In our present spectral range, the dielectric functions of the nanocrystalline film

are primarily ascribed to the fundamental optical transition. Moreover, for wide band gap FE materials, the dielectric response can be described by the contribution from typical critical point (CP). Therefore, the Adachi's model is employed to express the unknown dielectric functions of the BLT nanocrystalline film, and written as

$$\tilde{\varepsilon}(E) = \varepsilon_\infty + \frac{A_0\left[2 - \sqrt{1 + \chi_0(E)} - \sqrt{1 - \chi_0(E)}\right]}{\sqrt{E_0^3}\chi_0(E)^2}.$$ (6)

Here, $\chi_0 = (E + i\Gamma)/E_0$, A_0 and Γ are the strength and broadening values of the E_0 transition, respectively. (52) It should be emphasized that the dielectric functions of many semiconductor and dielectric materials have been successfully determined by fitting the Adachi's model to the measured data. (53; 54; 55; 56; 57; 58) On the other hand, the dielectric function of the metallic oxide films can be expressed using a Drude-Lorentz oscillator dispersion relation owing to the conductivity

$$\varepsilon(E) = \varepsilon_\infty - \frac{A_D}{E^2 + iEB_D} + \sum_{j=1}^{4}\frac{A_j}{E_j^2 - E^2 - iEB_j}.$$ (7)

Here ε_∞ is the high-frequency dielectric constant, A_j, E_j, B_j, and E is the amplitude, center energy, broadening of the jth oscillator, and the incident photon energy, respectively. (27; 29; 59) The refractive index n and extinction coefficient k can be calculated as follows

$$n = \frac{1}{\sqrt{2}}\sqrt{\sqrt{\varepsilon_1^2 + \varepsilon_2^2} + \varepsilon_1}, \quad k = \frac{1}{\sqrt{2}}\sqrt{\sqrt{\varepsilon_1^2 + \varepsilon_2^2} - \varepsilon_1}.$$ (8)

where ε_1 and ε_2 are the real part and imaginary part of the dielectric function, respectively. The root-mean-square fractional error σ, defined by

$$\sigma^2 = \frac{1}{N - M}\sum_{i=1}^{N}(T(R)_i^m - T(R)_i^c)^2.$$ (9)

where $T(R)_i^c$ and $T(R)_i^m$ are the calculated and measured values at the ith data point for the transmittance or reflectance spectra. N is the number of wavelength values and M is the number of free parameters. (11; 60; 61) A least squares-fitting procedure employing the modified Levenberg-Marquardt algorithm, the convergence of which is faster than that of the SIMPLEX algorithm, was used in the transmittance or reflectance spectral fitting.

4.2 SE technique

On other hand, SE, based on the reflectance configuration, provides a effective tool to extract simultaneously thickness and optical constants of a multilayer system. (48) It is a sensitive and nondestructive optical method that measures the relative changes in the amplitude and the phase of particular directions polarized lights upon oblique reflection from the sample surface. The experimental quantities measured by ellipsometry are the complex ratio $\tilde{\rho}(E)$ in terms of the angles $\Psi(E)$ and $\Delta(E)$, which are related to the structure and optical characterization of materials and defined as

$$\tilde{\rho}(E) \equiv \frac{\tilde{r}_p(E)}{\tilde{r}_s(E)} = \tan\Psi(E)e^{i\Delta(E)}.$$ (10)

here, $\tilde{r}_p(E)$ and $\tilde{r}_s(E)$ is the complex reflection coefficient of the light polarized parallel and perpendicular to the incident plane, respectively. (50) It should be noted that $\tilde{\rho}(E)$ is the function of the incident angle, the photon energy E, film thickness and optical constants $\tilde{n}(E)$, i.e., the refractive index n and extinction coefficient κ from the system studied. Generally, the pseudodielectric function $< \tilde{\varepsilon} >$ is a useful representation of the ellipsometric data Ψ and Δ by a two-phase (ambient/substrate) model (50)

$$< \tilde{\varepsilon} > = < \varepsilon_1 > + i < \varepsilon_2 > = \sin^2 \varphi \left\{ 1 + \left[\frac{1 - \tilde{\rho}}{1 + \tilde{\rho}} \right]^2 \tan^2 \varphi \right\}. \tag{11}$$

where φ is the incident angle. Although $\tilde{\rho}(E)$ and $\tilde{n}(E)$ may be transformed, there are no corresponding expressions for $\tilde{n}(E)$, which is distinct for different materials. (62) Therefore, the spectral dependencies of $\Psi(E)$ and $\Delta(E)$ have to be analyzed using an appropriate fitting model. Correspondingly, the film thickness d_f, optical constants and other basic physical parameters, such as optical band gap, the high frequency dielectric constant ε_∞, etc., can be extracted from the best fit between the experimental and fitted spectra. Similarly, the three-phase layered structure model cab be applied to reproduce the SE spectra of the LNO films on the Pt/Ti/SiO$_2$/Si substrates due to a smaller thickness (the maximum value is about 180 nm). In SE fitting, the root-mean-square fractional error, which is defined as

$$\sigma^2 = \frac{1}{2J - K} \sum_{i=1}^{J} \left[\left(\frac{\Psi_i^m - \Psi_i^c}{\sigma_{\Psi,i}^m} \right)^2 + \left(\frac{\Delta_i^m - \Delta_i^c}{\sigma_{\Delta,i}^m} \right)^2 \right]. \tag{12}$$

has been used to judge the quality of the fit between the measured and model data. (11) Where, J is the number of data points and K is the number of unknown model parameters, has been used to judge the quality of the fit between the measured and model data. Note that Eq. 12 has $2J$ in the pre-factor because there are two measured values included in the calculation for each and pair. The standard deviations were calculated from the known error bars on the calibration parameters and the fluctuations of the measured data over averaged cycles of the rotating polarizer and analyzer. Note that the same Levenberg-Marquardt algorithm as the above T or R data was applied to reproduce SE spectra. Therefore, the infrared optical constants of the LNO films can be uniquely extracted.

5. Optical properties of the BLT films

Typical transmittance spectra of the BLT films at different temperatures are shown in Fig. 2 (a). The spectra can be roughly separated into three specific regions: a transparent oscillating one (labeled with "I"), a low transmittance one ("II"), and a strong absorption one ("III") at higher photon energies. The Fabry-Pérot interference behavior observed in the transparent region, which is due to the multi-reflectance between the film and substrate, is similar to those on silicon substrates. (10; 63) The transmittance differences with the temperature are ascribed to the thermal expansion and variations of optical constants in lower photon energies. Transmittance spectra ranging from 80 to 480 K were measured in order to analyze the shift of the absorption edge during the phase transition. As shown in Fig. 3 (a), the spectral transmittance value sharply decreases with the photon energy and down to zero in the ultraviolet region beyond 4.5 eV. This is due to the strong absorption from the fundamental band gap and high-energy CP transitions, which can not be detected by the present transmittance spectra.
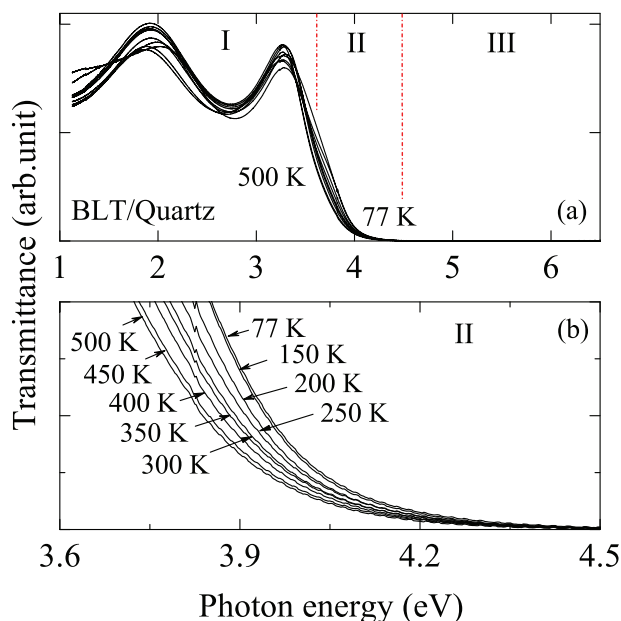
Fig. 2. Transmittance spectra of the BLT film at the temperature region from 77 to 500 K: (a) in the ultraviolet-infrared photon energy of 1.1-6.5 eV, and (b) near the OBG region of 3.6-4.5 eV. The arrows indicate the corresponding temperature values. (Figure reproduced with permission from (63). Copyright 2007, American Institute of Physics.)
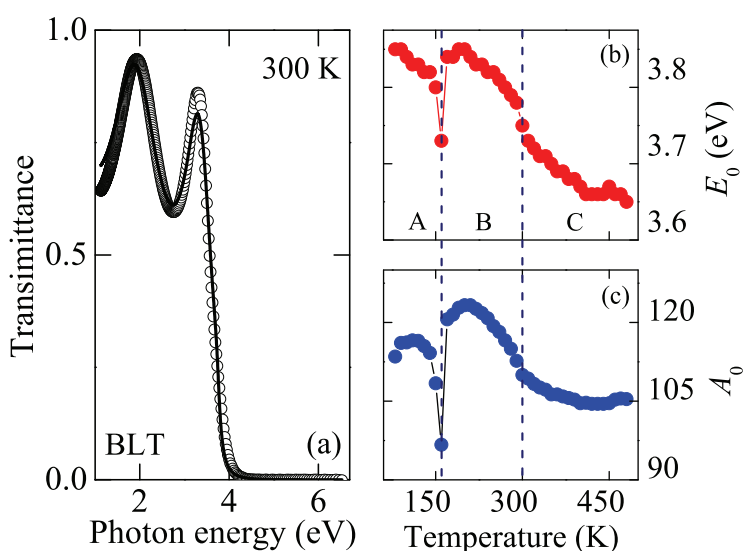

Fig. 3. (a) Experimental (dotted line) and fitting (solid line) transmittance spectra of the BLT film at 300 K. (b) The optical transition energy E_0 of the Adachi's model for the BLT film with different temperatures. It indicates that the optical transition energy E_0 decreases with increasing the temperature. Nevertheless, the anomalous behavior can be observed around 160 and 300 K. (c) The strength parameter A_0 of the E_0 transition with different temperatures.

Temperature (K)	A_0 (eV$^{3/2}$)	E_0 (eV)	Γ (eV)	S	E_c (eV)	E_d (eV)	$n(0)$
80	113.5	3.85	0.08	3.18	4.71	7.48	2.18
90	116.1	3.85	0.06	3.25	4.68	7.51	2.20
100	116.2	3.83	0.05	3.28	4.66	7.47	2.21
110	116.6	3.84	0.05	3.29	4.65	7.46	2.21
120	116.5	3.83	0.05	3.30	4.64	7.43	2.21
130	116.2	3.83	0.05	3.30	4.62	7.31	2.20
140	114.2	3.82	0.04	3.28	4.62	7.21	2.20
150	108.4	3.80	0.05	3.20	4.58	6.76	2.17
160	96.7	3.73	0.05	3.10	4.43	5.66	2.09
170	120.6	3.84	0.07	3.34	4.68	7.87	2.24
180	121.5	3.84	0.07	3.35	4.68	7.91	2.25
190	122.8	3.85	0.08	3.37	4.69	8.03	2.25
200	123.3	3.85	0.08	3.38	4.70	8.09	2.26
210	123.3	3.84	0.07	3.40	4.68	8.02	2.26
220	122.6	3.83	0.07	3.40	4.67	7.95	2.26
230	121.8	3.83	0.07	3.39	4.66	7.89	2.25
240	120.8	3.82	0.08	3.38	4.65	7.81	2.25
250	119.3	3.82	0.08	3.36	4.64	7.68	2.24
260	118.2	3.81	0.07	3.36	4.61	7.53	2.23
270	116.6	3.80	0.07	3.35	4.60	7.39	2.23
280	115.0	3.79	0.07	3.34	4.58	7.23	2.22
290	112.7	3.78	0.07	3.32	4.55	7.00	2.20
300	110.0	3.75	0.05	3.33	4.49	6.62	2.19
310	109.3	3.73	0.04	3.37	4.44	6.41	2.19
320	108.3	3.72	0.03	3.39	4.41	6.21	2.19
330	107.6	3.71	0.03	3.40	4.38	6.09	2.19
340	107.2	3.71	0.03	3.41	4.36	5.99	2.19
350	106.3	3.70	0.03	3.41	4.35	5.88	2.18
360	106.3	3.69	0.02	3.44	4.33	5.80	2.19
370	105.9	3.69	0.02	3.45	4.31	5.71	2.19
380	105.6	3.68	0.02	3.46	4.29	5.63	2.18
390	105.3	3.68	0.02	3.38	4.28	5.53	2.18
400	104.6	3.67	0.02	3.48	4.27	5.45	2.18
410	104.7	3.66	0.02	3.50	4.25	5.37	2.18
420	104.5	3.66	0.02	3.52	4.23	5.30	2.18
430	104.5	3.66	0.02	3.52	4.23	5.30	2.18
440	104.5	3.66	0.02	3.52	4.23	5.31	2.19
450	104.6	3.67	0.02	3.50	4.25	5.41	2.18
460	105.3	3.66	0.04	3.50	4.26	5.51	2.19
470	105.5	3.66	0.04	3.51	4.25	5.51	2.19
480	105.4	3.66	0.04	3.51	4.25	5.51	2.19

Table 1. The Adachi's model parameters of the BLT film at the temperature range of 80-480 K are determined from the simulation of the transmittance spectra. Note that the thickness is estimated to 145 nm and the ε_∞ is fixed to 1 for the film measured at different temperature. In addition, S, E_c, E_d, and $n(0)$ is the contribution from high-energy CP transitions, the oscillator energy, the dispersion energy of the Sellmeier relation, and long wavelength refractive index. respectively.

The fitted parameter values in Eq. 6 are summarized in Table 1 and Fig. 3 (b) and (c). A good agreement is obtained between the measured and calculated data in the experimental range, especially for the fundamental band gap region. For all temperatures, the fitting standard deviations are less than 2×10^{-3}. As can be seen in Fig. 3 (b), the optical transition energy E_0 of the BLT film increases with decreasing temperature except for the temperatures of 160 and 300 K. Fig. 3 (b) can be roughly separated into three specific regions: the monoclinic phase (labeled with "A"), the orthorhombi phase (labeled with "B") and the tetragonal phase (labeled with "C"). An obvious dip at 160 K for the fundamental band gap can be observed due to the phase/structural transition. (20) The origin of the structural anomaly is due to strain energy and lattice strain change with the temperature. The variation of E_0 with temperature can be mainly ascribed to thermal expansion and electron-phonon (e-p) interaction. The BLT film emits or absorbs the phonon with increasing temperature. It will result in the band gap perturbation and shift. The valence-band top mainly consists of the O_{2p} orbital, which is strongly hybridized with the Ti_{3d} orbital below the Fermi level. (13) The strong hybridization between the O_{2p} and Ti_{3d} orbitals changes with the distortion of the crystal structure during the phase transition. Therefore, the E_0 variation clearly indicates that the absorption edge is strongly related to the phase transition with decreasing temperature.

It is generally believed that the symmetry of BiT at RT is orthorhombic and changes to tetragonal at 675 °C. (64) As we know, physical properties of FE nanocrystals are strongly dependent on the grain size. (65) Recently, a size-driven phase transition was found at a critical size r_c of 44 nm for BiT. The high-temperature tetragonal phase stabilizes at RT when the grain size is smaller than the r_c. (17) According to the XRD analysis, the BLT film has the tetragonal crystal structure at RT. Various anomalies of BiT at low temperature are believed to be a possible indication of the structural transitions. For instance, the dielectric constant decreases with decreasing temperature except for a broad hump around about 150 K, the spontaneous polarization (P_s) changes little but for a gradual decrease in the 100-250 K range with some thermal hysteresis and the E_c gradually decreases to a minimum at 100 K except for the broad hump about 200 K. (20) The similar phenomena from the optical properties can be observed in the present BLT nanocrystalline film. Note that the parameter A_0 of the Adachi's model is anomalous at 160 and 300 K. Moreover, the E_0 continuously decreases with increasing temperature except for the values at the temperatures of 160 and 300 K. The dielectric function anomaly indicates that the BLT nanocrystalline film undergoes a tetragonal to orthorhombic phase transition in the temperature range of 200-250 K. (21) Thermodynamic analysis indicate that the energy separation of the orthorhombic and monoclinic states decreases with decreasing the temperature. (66) When the temperature further decreases, the BLT nanocrystalline film with orthorhombic structure undergoes monoclinic distortion around 160 K. (21) From the dielectric function model, one can safely conclude that the low temperature phase transition of the BLT film can be detected by the spectral transmittance.

The calculated dielectric functions are exhibited in Fig. 4. The real part ε_1 increases and reaches a maximum, beyond which it gradually falls with further increasing of the photon energy. The peak position of ε_1 corresponding approximately with the optical transition energy E_0 of the BLT film shifts to high energies with decreasing the temperature. The peaks may be assigned to the transitions between the CP or lines with high symmetry in the Brillouin zone, termed as Van Hove singularities. In the present case, the value of the photon energy corresponding to the peaks of ε_1 is about 3.7 eV, which agrees with the value of the FE band gap (3-4 eV). (67). Therefore, the CP may be associated with the interband transition between the valence and conduction bands of BLT nanocrystalline film. The sites of the dielectric
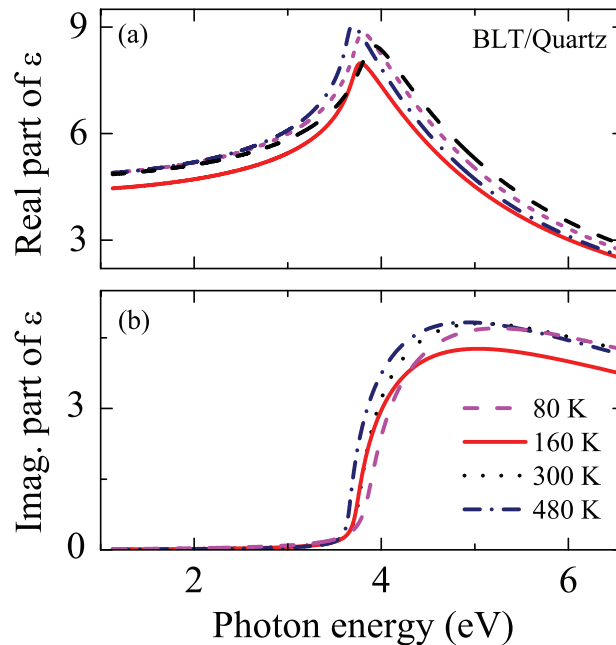
Fig. 4. Temperature dependence of dielectric function (a) real part and (b) imaginary part for the BLT nanocrystalline film in the photon energy range of 1.1-6.5 eV. The anomalies of dielectric function are observed at 160 and 300 K, respectively.

function or the refractive index peaks generally correspond to the band gap energies of the dielectrics and semiconductors. (68; 69) This can be understood from the K-K relation (70; 71)

$$n(v) = 1 + \frac{c}{\pi} \int \frac{d\alpha(v')}{dv'} \log(\frac{v' + v}{v' - v}) dv'. \tag{13}$$

where c is the light velocity in vacuum, v and v' are light frequencies, $\alpha(v')$ is the absorption coefficient. In the frequency region near the absorption edge the value of $d\alpha(v')/dv'$ is very large; however, when the photon energy reaches the gap energy, the absorption curve changes its slope and becomes smoother, so the value of $d\alpha(v')/dv'$ decreases at the absorption edge. The imaginary part ε_2 is nearly zero in the interference region and increases rapidly with E, reaches a maximum, and falls slightly at higher energies. The ε_2 near the fundamental band gap energy is not zero due to defects and disorder in the nanocrystalline film. Moreover, the real part of ε decreases with the temperature and varies from 9.04 at 480 K to 8.22 at 80 K at the photon energy of 3.7 eV. The reduction is due to decreasing electron-phonon interactions at degraded temperatures, making direct transitions less probable. From Fig. 4, an anomaly of the dielectric function is observed at 160 and 300 K, which can be ascribed to the phase/strucutral transitions. Fig. 5 exhibits the temperature-dependent refractive index n at various photon energies. The anomalous variations occur at the temperature rang of 130-160 K and 290-330 K, indicating the subtle phase transitions in the corresponding temperature regions, as compared with lower-temperature Raman results. (20; 21) As previously discussed, the optical constants are strongly related to the crystalline structure, which can affect the valence and conduction band formation. Obviously, the structural variation of the BLT film can contribute to the optical response.
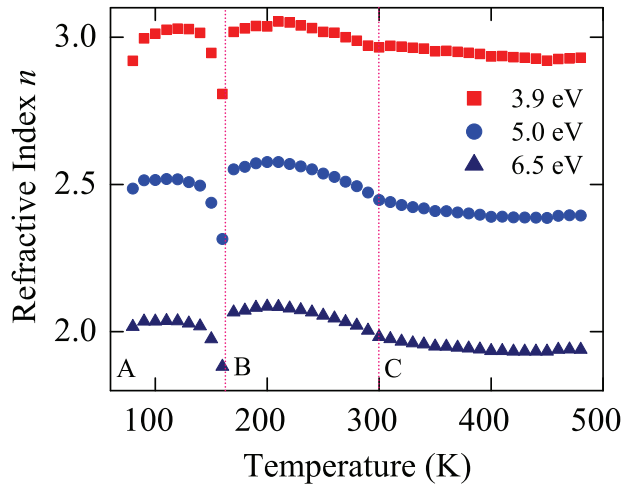
Fig. 5. Variation of the refractive index for the BLT nanocrystalline film with the temperature at the photon energies of 3.9, 5, and 6 eV, respectively.

In order to give an insight on the electronic band structure of the BLT film, we have fitted the refractive index n below the optical transition energy with a dispersion formula corresponding to an empirical Sellmeier equation

$$n^2 = S + \frac{E_c E_d}{E_c^2 - E^2}.$$

(14)

Here, S is the contribution from high-energy CP transitions, E_c the oscillator energy, and E_d the dispersion energy. The fitting quality from the BLT film at 80 K has been illustrated in Fig. 6 (a). The empirical Sellmeier equation gives a relatively good description to the optical
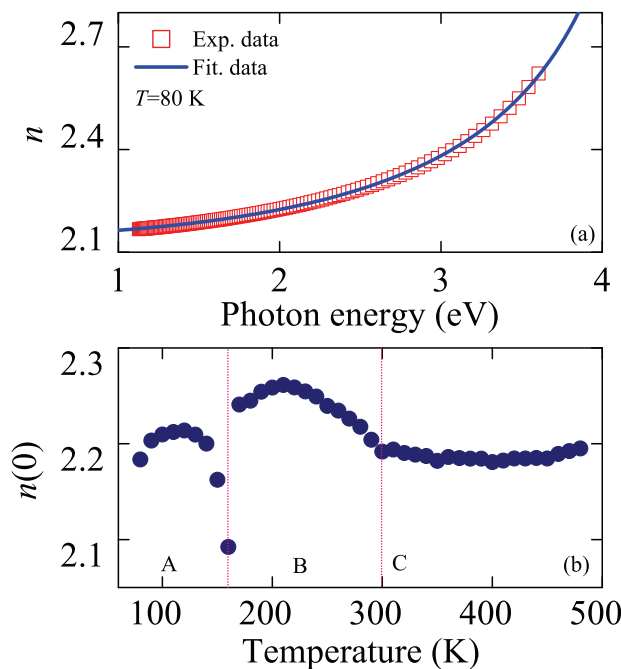
Fig. 6. (a) An empirical Sellmeier equation in the transparent region for BLT nanocrystalline film at 80 K. (b) The long wavelength refractive index $n(0)$ with different temperatures. The anomalous $n(0)$ values occur at 160 and 300 K, respectively.
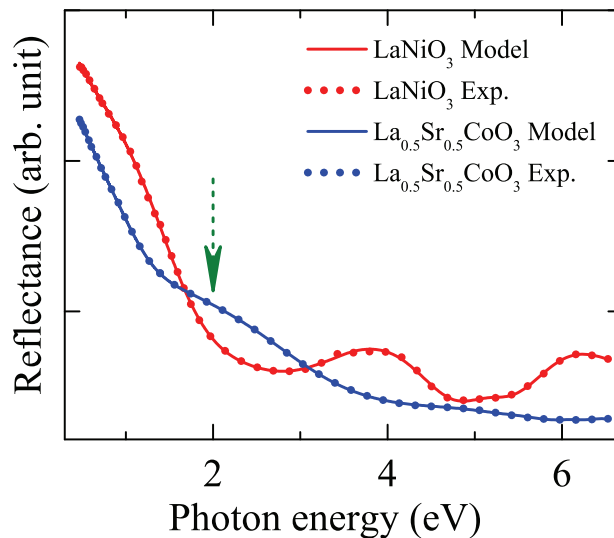
Fig. 7. Experimental (dotted lines) and best-fit (solid lines) near-normal incident reflectance spectra of LNO and $La_{0.5}Sr_{0.5}CoO_3$ films. The arrow is applied to approximately distinguish two different electronic transition regions. (Figure reproduced with permission from (25). Copyright 2009, American Institute of Physics.)

dispersion in the transparent range. The parameters of Sellmeier equation are summarized in Table 1. The *S* value generally increases with the temperature except for the phase transitions, indicating that the effects from high-frequency electronic transitions becomes stronger in the BLT film. It can be found that the maximum optical transition occurs near the energy range of 4.2-4.7 eV from the fitted oscillator energy, which agrees well with ε_2 observed (see Fig. 4). It indicates that the optical dispersion in the transparent region is mainly ascribed to the higher CP virtual transitions and not by the band gap energy. Note that the parameter *S* presents an opposite variation trend with the temperature, as compared with the oscillator energy E_c and the dispersion energy E_d apart from the temperature ranges around 160 and 300 K. Again, the anomaly can be ascribed to the phase transitions as previously discussed. The long wavelength refractive index $n(0)$, which can be calculated from $\sqrt{(E_d/E_c) + S}$, is shown in Fig. 6 (b). The $n(0)$ at 300 K is estimated to be about 2.19 at zero point, which indicates that the dielectric function is about 4.80. The $n(0)$ is related to the total effective number of valence electrons per atom in materials. For theoretically calculating $n(0)$, the f-sum-rule integral can be written as

$$n^2(0) - 1 = \frac{4}{\pi} \int_0^\infty \frac{n(\omega')k(\omega')}{\omega'} d\omega'. \tag{15}$$

It indicates that the long wavelength refractive index is smaller for materials with wider fundamental band gap because there is lower energy transition possibility, which results in less contributions to the imaginary part of dielectric function $[n(w)k(w)]$. In addition, the band gap of the present BLT nanocrystalline film could be larger due to the crystalline size effect, as compared to that of bulk crystal. (72; 73) Thus, the $n(0)$ will be further decreased. Although the phase transitions of the BLT film can be controlled by the crystalline/grain effect, the present transmittance spectra at variable temperature further indicate that the subtle phase transitions appear in the nanocrystalline film structure.

Samples	Lorentz (j)	A_j (eV)^2	E_j (eV)	B_j (eV)
LNO	1	1.97 (0.09)	2.32 (0.02)	2.28 (0.05)
	2	2.0 (0.1)	3.36 (0.01)	2.16 (0.06)
	3	0.19 (0.01)	5.10 (0.02)	0.9 (0.1)
	4	2.69 (1.07)	7.31 (0.41)	3.29 (0.93)
La$_{0.5}$Sr$_{0.5}$CoO$_3$	1	0.33 (0.06)	1.55 (0.01)	1.22 (0.06)
	2	2.31 (0.06)	2.11 (0.04)	3.06 (0.06)
	3	1.57 (0.07)	4.59 (0.01)	3.03 (0.07)
	4	0.10 (0.02)	6.01 (0.03)	0.73 (0.10)

Table 2. The Lorentz oscillator parameter values of LNO and La$_{0.5}$Sr$_{0.5}$CoO$_3$ films are determined from the simulation of reflectance spectra. The 90% reliability of the fitting parameters is given with the parentheses. (Table reproduced with permission from (25). Copyright 2009, American Institute of Physics.)

6. Electronic band structures of the LNO and LSCO films

The experimental reflectance spectra of the LNO and LSCO films are shown in Fig. 7 with the dotted lines. Generally, the reflectance spectra recorded show the similar dependence on the photon energy except for the amplitude, which is slightly higher in the LNO film. Note that the reflectance spectrum from the LSCO film is similar to that of the film grown on MgO substrate, where a slight dip appears from optical reflectance measurement. (74) The reflectance spectra can be roughly divided into two regions (see the dotted line in Fig. 7). The lower photon energy region below about 2 eV is assigned to a strong Drude response, which is derived from the intraband transition of free carrier. It was reported that the typical energy scale of the Jahn-Teller (JT) related excitations are varied between 0.5 and 3 eV. (75) It indicates that the Ni^{3+} and Co^{3+} ions related JT effect is important in the perovskite-type materials, whose lattice distortion can couple via an orbital exciton strongly in the 3d correlated metallic systems. (37) The results are similar to some high temperature superconductors. (75) The charge-transfer excitations are located above 2.0 eV for the LNO and LSCO films. The interband electronic transitions are mainly derived from O 2p and Ni/Co 3d energy states. (38) It was argued that the crystal field splitting and the JT effect in the metallic oxides can affect the charge-transfer transitions. (75)

In order to clarify the different transition energy bands, the Lorentz oscillator model expressing the respective contribution to the optical response is necessary. The reproduced optical reflectance results with the Drude-Lorentz model are also shown in Fig. 7 by the solid lines and the parameter values are given in Table 2. A good agreement is obtained between the experimental and calculated spectra in the entirely measured photon energy region. In particular, the oscillator broadening are generally less than the corresponding E_j values (see Table 2), indicating that the Drude-Lorentz dispersion is reliable and satisfying, similar to the results from some metal films. (28) It is testified that four Lorentz oscillators are requisite for the nanocrystalline films, as compared with some noble metal films. (28) These Lorentz oscillators can correspond to different interband electronic transitions, respectively. For the LNO material, the optical transition peaks are located at 2.32 ± 0.02, 3.36 ± 0.01, 5.10 ± 0.02, and 7.31 ± 0.41 eV. These center energy positions can be readily distinguished from the reflectance spectrum. For the LSCO film, however, the four center energy peaks are found at 1.55 ± 0.01, 2.11 ± 0.04, 4.59 ± 0.01, and 6.01 ± 0.03 eV, respectively. Compared with the result of the LNO film, these transition energy positions are overlapped on the reflectance
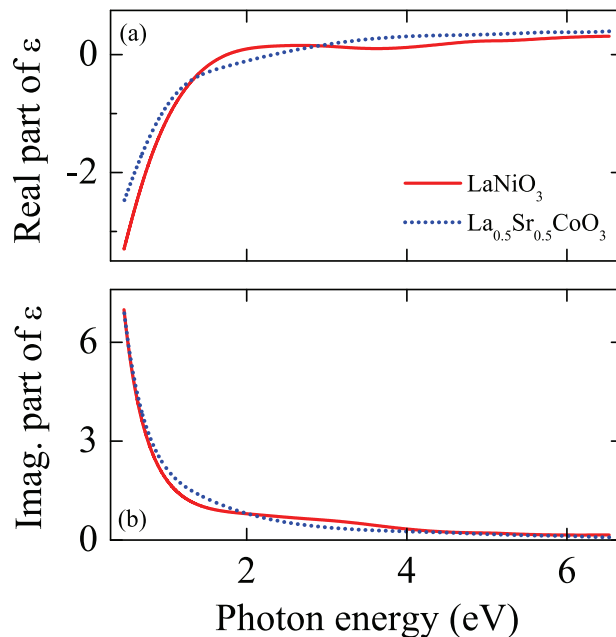
Fig. 8. The real part (a) and imaginary part (b) of dielectric function in LaNiO$_3$ and La$_{0.5}$Sr$_{0.5}$CoO$_3$ films from infrared to ultraviolet photon energy regions. (Figure reproduced with permission from (25). Copyright 2009, American Institute of Physics.)

spectrum due to the large broadening. As compared with the theoretical model of the band structure for the metallic oxides, (75; 76; 77) the four energy bands can be assigned to the following electronic transitions: (1) O 2p to Ni/Co 3d (t_{2g}-JT); (2) O 2p to Ni/Co 3d (t_{2g}+JT); (3) O 2p to Ni/Co 3d (e_g-JT); and (4) O 2p to Ni/Co 3d (e_g+JT), respectively. The results are in good agreement with the data from the photoemission spectroscopy, in which four prominent band structures can be observed above the Fermi level (E_F). (38) Based on the Drude model parameters, it can be found that the plasma frequency of the LSCO film (A_D is 3.47 ± 0.04 eV) is slightly larger than that from the LNO film (A_D is 3.34 ± 0.03 eV). Note that the parameter B_D is 0.74 ± 0.01 eV and 0.84 ± 0.01 eV for the LNO and LSCO films, respectively. The phenomena can be confirmed from the reflectance spectra.

From the model parameters, the dielectric constants can be readily obtained. The evolution of $\tilde{\varepsilon}(E)$ with the photon energy for the LNO and LSCO films is shown in Fig. 8 (a) and (b). Generally, the real part ε_r increases with the photon energy and the values for LNO and LSCO films are evaluated to be about -3.3 and -2.5 at 0.47 eV, respectively. Note that the ε_r of the LSCO film is slightly larger than that of the LNO film in the mid-infrared region. According to the Drude model, the free carrier results in the fact that the dielectric constant decreases to a high negative value as photon energy approaches zero. (28) It indicates that the contribution from the Drude response becomes more prominent for the LSCO material, which agrees well with the above analysis on the plasma frequency. On the other hand, the imaginary part ε_i strikingly decreases with the photon energy and approaches zero towards the ultraviolet energy region, indicating the contributions from the strong interband transitions. Note that the ε_i is slightly smaller that those of nobel metal films. The ε_i discrepancy between the LNO and LSCO films is not obvious, as compared with the ε_r. It can be attributed to the fact that they have the similar perovskite crystalline structure.

In order to give a further insight on the electronic structure of the LNO and LSCO films, the real part of optical conductivity σ can be calculated by $\sigma_r = \varepsilon_0 \omega \varepsilon_i$, here ε_0 and ω is the
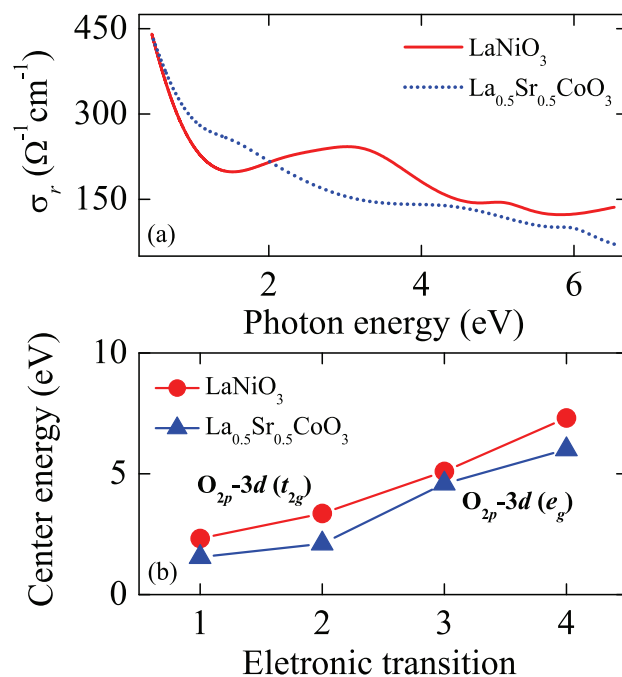
Fig. 9. The comparison of the optical conductivity between two films (a) and (b) the Lorentz oscillator E_j value corresponds to the electronic transitions from O $2p$ to Ni/Co $3d$, respectively. (Figure reproduced with permission from (25). Copyright 2009, American Institute of Physics.)

vacuum dielectric constant and the light frequency, respectively. Fig. 9 (a) gives a comparison of the σ_r for the LNO and LSCO films. Although the σ_r is approximately varied from 100 to 450 Ω^{-1}cm^{-1}, the optical conductivity presents a different behavior for the perovskite-type oxide materials. In the mid-infrared region, the σ_r rapidly increases with decreasing photon energy because of the contribution from the Drude response. Then the optical conductivity rapidly decreases with further increasing the photon energy. From the visible to ultraviolet energy regions, the absorption peaks owing to the interband electronic transitions can be easily distinguished for the LNO film, compared with the LSCO film. Note that the conductive behavior for the two samples is similar to those of high-temperature superconductivity. (74) Fig. 9 (b) shows the four energy bands for the charge-transfer excitations. Considering the corresponding electronic structure, the transition energy of the LNO film is slightly larger than those of the LSCO film. The small discrepancy is mainly due to Ni or Co $3d$ electronic states for the LNO and LSCO materials, respectively. Owing to the distinct $3d$ orbital energy, the t_{2g} and e_g states can be located at different level in the energy space, which induces the center energy variation for two perovskite-type oxides. Note that the La and/or Sr composition ratio can affect the O_{2p} and $3d$ orbital distributions as well. (75) It was reported that the structural distortions can affect the electronic band structures of the perovskite material. (77; 63) Therefore, the highly preferential orientation LNO and polycrystalline LSCO layers can contribute to the changed electronic structure. In addition, the LNO and LSCO films have different grain size, which results in the grain boundary discrepancy and maybe further affect the electronic state.
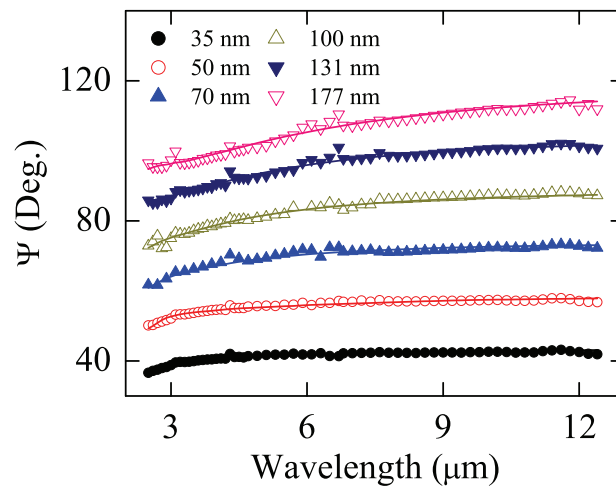
Fig. 10. Experimental (dotted lines) and fitted ellipsometric (solid lines) Ψ spectra of the LNO films with different film thickness at the incident angle of 75°. (Figure reproduced with permission from (47). Copyright 2003, The Japan Society of Applied Physics.)

7. Infrared optical constants of the LNO films

As an example, the measured Ψ and Δ spectra at the incident angle of 75° for the LNO films on $Pt/Ti/SiO_2/Si$ substrates in the wavelength range of 2.5-12.5 μm are shown by the dotted lines in Figs. 10 and 11, respectively. In order to estimate the infrared optical constants of the LNO films, the ellipsometric spectra were analyzed by a three-phase (Air/LNO/Pt) model system as the Pt layers were thick enough that the infrared light could not propagate through them. (50) The unknown infrared optical constants of the LNO films were described using the Drude model, i.e., the first term of Eq. 7. The optical constants of Pt in the fitting were taken from Ref. (62). The infrared optical constants of the LNO films were determined by fitting the model function to the measured data. Note that the fitted film thicknesses are in good agreement with the measured values by scanning electron microscopy within the experimental error bars. The Ψ and Δ spectra are shown in Figs. 10 and 11 by the solid lines, respectively. The best fit is obtained between the measured data and the model fit in the entirely measured wavelength range.

The evaluated optical constants n and κ of the LNO films are shown in Fig. 12 (a) and (b), respectively. The refractive index and extinction coefficient of the LNO films increase with increasing the wavelength, which indicates that $LaNiO_3$ is of some metallic characteristics. In addition, the refractive index of the LNO films decreases with increasing the thickness in the entirely measured wavelength range except for two thinner samples in the short wavelengths. However, the extinction coefficient of the LNO films monotonously decreases with increasing the thickness in the entirely measured wavelength range. In particular, the difference of the infrared optical constants decreases with increasing the thickness. It indicates that the optical properties of films are close to those of bulk materials with increasing the thickness. The value of the refractive index decreases from 10.4 to 1.41, and the extinction coefficient decreases from 14.5 to 1.15 with increasing the thickness in the wavelength of 12.5 μm. It is believed that the crystallinity of the films results in the thickness dependence of the infrared optical properties. From the XRD patterns of the LNO films (not shown), the crystallinity of the LNO films is improved with increasing the thickness. (47) It is possible that the thinner films contained

a small fraction of amorphous phase, which remained undetected by XRD. To explain this deviation, the assumption that the change in the structure and texture sensitively reflects the refractive index is presented. In this case, the shift of the optical constants should be limited by the difference between the optical constants for the crystalline and amorphous phases, leading to a large shift of the infrared optical properties. (78; 79) The XRD measurements show that the full width at half maximum (FWHM) of the (200) peak in the LNO films are $0.341°$, $0.358°$ and $0.346°$ for the 100-nm, 131-nm and 177-nm thick films, respectively. However, the peak positions do not shift with decreasing thickness except for the 177-nm thick films, the (200) diffraction peak of which shifts the smaller angle side.

The interaction between the grain boundaries and/or morphologies and the infrared light increases with increasing grain size, which can be changed as the thickness. It can induce the difference of the optical constants with increasing the thickness. On the other hand, the influence of the interface layer may be responsible for the observed deviation. Although there is the sharp interface feature between LNO and Pt substrates, the stress may lie in the interface because of the difference from the coefficient of thermal expansion between LNO and Pt. The stress or strain can affect not only the crystallinity of the LNO films, but also the infrared optical properties. Because the LNO films are semi-transparent in the measured wavelength region, the reflected light has the interaction to the interface layer. With increasing thickness, the effect of the interface layer could increase and induce the change of the detected light, and finally result in the difference of the infrared optical properties. Therefore, we believe that the difference of the infrared optical properties is due mainly to the crystalline size effect, the influence of the interface layer and existence of some amorphous phases in the films. In addition, the IRSE data do not reveal sensitivity to surface roughness, because scattering becomes inefficient for long wavelengths. (80) The change of the surface roughness with different film thickness can affect the infrared optical properties of the LNO thin films because the influence (such as lower refractive index and extinction coefficient) of the surface roughness has been added in the optical properties. Therefore, the LNO films approach the bulk behavior and show the metallic properties with increasing the thickness from the IRSE experiments.
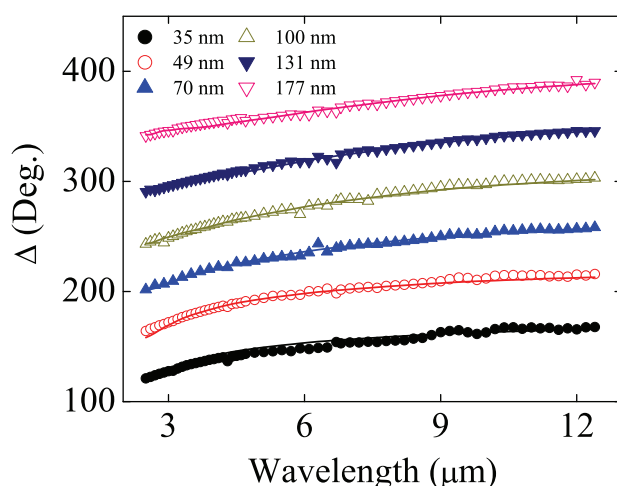

Fig. 11. Experimental (dotted lines) and fitted ellipsometric (solid lines) Δ spectra of the LNO films with different film thickness at the incident angle of $75°$. (Figure reproduced with permission from (47). Copyright 2003, The Japan Society of Applied Physics.)
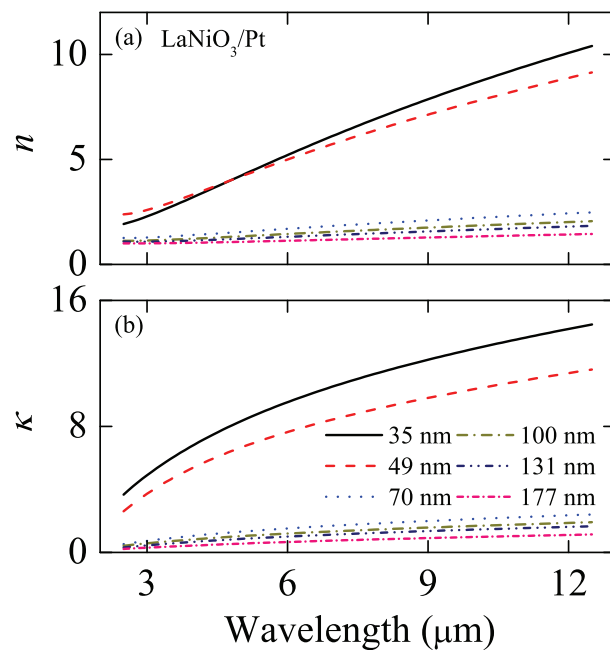
Fig. 12. The fitted spectroscopic dispersion of the optical constants (a) *n* and (b) *κ* of the LNO films with different film thickness. (Figure reproduced with permission from (47). Copyright 2003, The Japan Society of Applied Physics.)

8. Conclusion

In summary, the temperature influence on the optical properties of the BLT film prepared by chemical solution method on quartz substrate has been studied by the transmittance measurements. The Adachi's model has been employed to calculate the dielectric functions. The temperature dependence of the refractive index dispersion below the transition energy is found to obey an empirical Sellmeier equation. The results indicate that the BLT film transforms from tetragonal to orthorhombic structure in the temperature range 300-160 K, and then undergoes the orthorhombic to monoclinic transition with further decreasing the temperature. The traditional spectral transmittance technique provide a novel solution to observing the phase transitions of FE materials. On the other hand, the dielectric functions of high-quality LNO and LSCO conductive oxide films have been investigated by fitting the reflectance spectra and ellipsometric spectra with the Drude-Lorentz model. The optical conductivity presents a different behavior for two perovskite-type oxides due to the contributions from the charge-transfer excitations. Moreover, the crystallinity of the films results in the thickness dependence of the infrared optical properties. The present results indicate that the spectral techniques can be successfully used to study the optical properties of the perovskite-type FE and conductive metal oxide films. The experimental data could be crucial for the applications from the FE-based optoelectronic devices.

Although the optical properties, such as optical constants, optical band gap and electronic band structures of the perovskite-type FE and conductive metallic oxides have been discussed with the aid of the transmittance, reflectance and spectroscopic ellipsometry methods in this chapter, the external field (i.e., electrical and/or magnetic fields) effects on the optical properties of these oxide materials are still kept as an open issue. In order to easily operating the optoelectronic devices, the influences must be addressed before the "actual" devices can be applied. The projects will be developed in the near future.

9. Acknowledgments

10. References

[1] Lee, H. N.; Hesse, D.; Zakharov, N. & Gösele, U. (2002). Ferroelectric $Bi_{3.25}La_{0.75}Ti_3O_{12}$ films of uniform *a*-axis orientation on silicon substrates. *Science*, 296, 5575, 2006-2009

[2] Ahn, C. H.; Rabe, K. M. & Triscone, J. -M. (2004). Ferroelectricity at the nanoscale: Local polarization in oxide thin films and heterostructures. *Science*, 303, 5657, 488-491

[3] Yeh, C. S. & Wu, J. M. (2008). Characterization of $Pt/multiferroic BiFeO_3/(Ba,Sr)TiO_3/Si$ stacks for nonvolatile memory applications. *Appl. Phys. Lett.*, 93, 15, 154101(1-3)

[4] Scott, J. F. (2007). Applications of modern ferroelectrics. *Science*, 315, 5814, 954-959

[5] Catalan, G. & Scott, J. F. (2009). Physics and applications of bismuth ferrite. *Adv. Mater.*, 21, 24, 2463-2485

[6] Kan, Y.; Liu, Y. F.; Mieth, O.; Bo, H. F.; Wu, X. M.; Lu, X. M.; Eng, L. M. & Zhu, J. S. (2009). Mechanical stress induced polarization reorientation in polycrystalline $Bi_{3.25}La_{0.75}Ti_3O_{12}$ films. *Phys. Lett. A*, 374, 2, 360-365

[7] Cummins, S. E. & Cross, L. E. (1968). Electrical and optical properties of ferroelectric $Bi_4Ti_3O_{12}$ single crystals. *J. Appl. Phys.*, 39, 5, 2268-2274

[8] Scott, J. F. & Paz de Araujo, C. A. (1989). Ferroelectric memories. *Science*, 246, 4936, 1400-1405

[9] Park, B. H.; Kang, B. S.; Bu, S. D.; Noh, T. W.; Lee, J. & Jo, W. (1999). Lanthanum-substituted bismuth titanate for use in non-volatile memories. *Nature*, 401, 6754, 682-684

[10] Hu, Z. G.; Ma, J. H.; Huang, Z. M.; Wu, Y. N.; Wang, G. S. & Chu, J. H. (2003). Dielectric functions of ferroelectric $Bi_{3.25}La_{0.75}Ti_3O_{12}$ thin films on Si(100) substrates. *Appl. Phy. Lett.*, 83, 18, 3686-3688

[11] Hu, Z. G.; Wang, G. S.; Huang, Z. M. & Chu, J. H. (2003). Optical properties of $Bi_{3.25}La_{0.75}Ti_3O_{12}$ thin films using spectroscopic ellipsometry. *J. Appl. Phys.*, 93, 7, 3811-3815

[12] Du, H. C.; Tang, L. J. & Kaskel, S. (2009). Preparation, microstructure, and ferroelectric properties of $Bi_{3.25}La_{0.75}Ti_{3-x}M_xO_{12}$ (M = Mo, W, Nb, V) ceramics. *J. Phys. Chem. C*, 113, 4, 1329-1339

[13] Shimakawa, Y.; Kubo, Y.; Tauchi, Y.; Asano, H.; Kamiyama, T.; Izumi, F. & Hiroi, Z. (2001). Crystal and electronic structures of $Bi_{4-x}La_xTi_3O_{12}$ ferroelectric materials. *Appl. Phys. Lett.*, 79, 17, 2791-2793

[14] Spanier, J. E.; Kolpak, A. M.; Urban, J. J.; Grinberg, I.; Lian, Q. Y.; Yun, W. S.; Rappe A. M. & Park, H. (2006). Ferroelectric phase transition in individual single-crystalline $BaTiO_3$ nanowires. *Nano Lett.*, 6, 4, 735-739

[15] Sirenko, A. A.; Bernhard, C.; Golnik, A.; Clark, A. M.; Hao, J. H.; Si, W. D. & Xi, X. X. (2000). Soft-mode hardening in $SrTiO_3$ thin films. *Nature*, 404, 6776, 373-376

[16] Tenne, D. A.; Bruchhausen, A.; Lanzillotti-Kimura, N. D.; Fainstein, A.; Katiyar, R. S.;

Cantarero, A.; Soukiassian, A.; Vaithyanathan, V.; Haeni, J. H.; Tian, W.; Schlom, D. G.; Choi, K. J.; Kim, D. M.; Eom, C. B.; Sun, H. P.; Pan, X. Q.; Li, Y. L.; Chen, L. Q.; Jia, Q. X.; Nakhmanson, S. M.; Rabe, K. M. & Xi, X. X. (2006). Probing nanoscale ferroelectricity by ultraviolet Raman spectroscopy. *Science*, 313, 5793, 1614-1616

[17] Du, Y. L.; Zhang, M. S.; Chen, Q.; Yuan, Z. R.; Yin, Z. & Zhang, Q. A. (2002). Size effect and evidence of a size-driven phase transition in $Bi_4Ti_3O_{12}$ nanocrystals. *Solid State Commun.*, 124, 3, 113-118

[18] RÍos, S.; Scott, J. F.; Lookman, A.; McAneney, J.; Bowman, R. M.; & Gregg, J. M. (2006). Phase transitions in epitaxial $Ba_{0.5}Sr_{0.5}TiO_3$ thin films. *J. Appl. Phys.*, 99, 2, 024107(1-8)

[19] Hoshina, T.; Kakemoto, H.; Tsurumi, T.; Wada, S. & Yashima, M. (2006). Size and temperature induced phase transition behaviors of barium titanate nanoparticles. *J. Appl. Phys.*, 99, 5, 054311(1-8)

[20] Idink, H.; Srkanth, V.; White, W. B. & Subbarao, E. C. (1994). Raman study of low temperature phase transitions in bismuth titanate, $Bi_4Ti_3O_{12}$. *J. Appl. Phys.*, 76, 3, 1819-1823

[21] Du, Y. L.; Chen, G. & Zhang, M. S. (2004). Grain size effects in $Bi_4Ti_3O_{12}$ nanocrystals investigated by Raman spectroscopy. *Solid State Commun.*, 132, 3-4, 175-179

[22] Sohn, J. I.; Joo, H. J.; Ahn, D.; Lee, H. H.; Porter, A. E.; Kim, K.; Kang, D. J. & Welland, M. E. (2009). Surface-stress-induced Mott transition and nature of associated spatial phase transition in single crystalline VO_2 nanowires. *Nano Lett.*, 9, 10, 3392-3397

[23] Tenne, D. A.; Turner, P.; Schmidt, J. D.; Biegalski, M.; Li, Y. L.; Chen, L. Q.; Soukiassian, A.; Trolier-McKinstry, S.; Schlom, D. G.; Xi, X. X.; Fong, D. D.; Fuoss, P. H.; Eastman, J. A.; Stephenson, G. B.; Thompson, C. & Streiffer, S. K. (2009). Ferroelectricity in ultrathin $BaTiO_3$ films: Probing the size effect by ultraviolet Raman spectroscopy. *Phy. Rev. Lett.*, 103, 17, 177601(1-4)

[24] Zhang, S. X.; Chou, J. Y. & Lauhon, L. J. (2009). Direct correlation of structural domain formation with the metal insulator transition in a VO_2 nanobeam. *Nano Lett.*, 9, 12, 4527-4532

[25] Hu, Z. G.; Li, W. W.; Li, Y. W.; Zhu, M.; Zhu, Z. Q. & Chu, J. H. (2009). Electronic properties of nanocrystalline $LaNiO_3$ and $La_{0.5}Sr_{0.5}CoO_3$ conductive films grown on silicon substrates determined by infrared to ultraviolet reflectance spectra. *Appl. Phys. Lett.*, 94, 22, 221104(1-4)

[26] Yang, B.; Aggarwal, S.; Dhote, A. M.; Song, T. K.; Ramesh, R. & Lee, J. S. (1997). $La_{0.5}Sr_{0.5}CoO_3/Pb(Nb_{0.04}Zr_{0.28}Ti_{0.68})O_3/La_{0.5}Sr_{0.5}CoO_3$ thin film heterostructures on Si using TiN/Pt conducting barrier [capacitors]. *Appl. Phys. Lett.*, 71, 3, 356-358

[27] Hu, Z. G.; Huang, Z. M.; Wu, Y. N.; Zhao, Q.; Wang, G. S. & Chu, J. H. (2004). Ellipsometric characterization of $LaNiO_{3-x}$ films grown on Si(111) substrates: Effects of oxygen partial pressure. *J. Appl. Phys.*, 95, 8, 4036-4041

[28] Choi, W. S.; Seo, S. S. A.; Kim, K. W.; Noh, T. W.; Kim, M. Y. & Shin, S. (2006). Dielectric constants of Ir, Ru, Pt, and IrO2: Contributions from bound charges. *Phys. Rev. B*, 74, 20, 205117(1-8)

[29] Berini, B.; Keller, N.; Dumont, Y.; Popova, E.; Noun, W.; Guyot, M.; Vigneron, J.; Etcheberry, A.; Franco, N. & M. C. da Silva, R. (2007). Reversible phase transformation of $LaNiO_{3-x}$ thin films studied in situ by spectroscopic ellipsometry. *Phys. Rev. B*, 76, 20, 205417(1-9)

[30] Rossel, C.; Rosová, A.; Hušeková, K.; Machajdík, D. & Fröhlich, K. (2006). Phase stability of $La_{0.5}Sr_{0.5}CoO_{3-y}$ films upon annealing in hydrogen atmosphere. *J. Appl. Phys.*, 100,

4, 044501(1-6)

[31] Xie, C. K.; Budnick, J. I.; Wells, B. O. & Woicik, J. C. (2007). Separation of the strain and finite size effect on the ferromagnetic properties of La$_{0.5}$Sr$_{0.5}$CoO$_3$ thin films. *Appl. Phys. Lett.*, 91, 17, 172509(1-3)

[32] Noun, W.; Berini, B.; Dumont, Y.; Dahoo, P. R. & Keller, N. (2007). Correlation between electrical and ellipsometric properties on high-quality epitaxial thin films of the conductive oxide LaNiO$_3$ on STO (001). *J. Appl. Phys.*, 102, 6, 063709(1-7)

[33] Mambrini, G. P.; Leite, E. R.; Escote, M. T.; Chiquito, A. J.; Longo, E.; Varela, J. A. & Jardim, R. F. (2007). Structural, microstructural, and transport properties of highly oriented LaNiO$_3$ thin films deposited on SrTiO$_3$(100) single crystal. *J. Appl. Phys.*, 102, 4, 043708(1-6)

[34] Angadi, M.; Auciello, O.; Krauss, A. R. & Gundel, H. W. (2000). The role of electrode material and polarization fatigue on electron emission from ferroelectric Pb(Zr$_x$Ti$_{1-x}$)O$_3$ cathodes. *Appl. Phys. Lett.*, 77, 17, 2659-2661

[35] Naumov, I. I.; Bellaiche, L. & Fu, H. X. (2004). Unusual phase transitions in ferroelectric nanodisks and nanorods. *Nature*, 432, 7018, 737-740

[36] Kim, J.; Yang, S. A.; Choi, Y. C.; Han, J. K.; Jeong, K. O.; Yun, Y. J.; Kim, D. J.; Yang, S. M.; Yoon, D.; Cheong, H.; Chang, K. -S.; Noh, T. W. & Bu, S. D. (2008). Ferroelectricity in highly ordered arrays of ultra-thin-walled Pb(Zr,Ti)O$_3$ nanotubes composed of nanometer-sized perovskite crystallites. *Nano Lett.*, 8, 7, 1813-1818

[37] Sreedhar, K.; Honig, J. M.; Darwin, M.; McElfresh, M.; Shand, P. M.; Xu, J.; Crooker, B. C. & Spalek, J. (1992). Electronic properties of the metallic perovskite LaNiO$_3$: Correlated behavior of 3d electrons. *Phys. Rev. B*, 46, 10, 6382-6386

[38] Horiba, K.; Eguchi, R.; Taguchi, M.; Chainani, A.; Kikkawa, A.; Senba, Y.; Ohashi, H. & Shin, S. (2007). Electronic structure of LaNiO$_{3-x}$: An in situ soft x-ray photoemission and absorption study. *Phys. Rev. B*, 76, 15, 155104(1-6)

[39] Kuhns, P. L.; Hoch, M. J. R.; Moulton, W. G.; Reyes, A. P.; Wu, J. & Leighton, C. (2003). Magnetic phase separation in La$_{1-x}$Sr$_x$CoO$_3$ by ^{59}Co nuclear magnetic resonance. *Phys. Rev. Lett.*, 91, 12, 127202(1-4)

[40] Heaven, O. S. (1991). *Optical Properties of Thin Solid Films*, Dover, NewYork

[41] Hu, Z. G.; Huang, Z. M.; Wu, Y. N.; Hu, S. H.; Wang, G. S.; Ma, J. H. & Chu, J. H. (2004). Optical characterization of ferroelectric Bi$_{3.25}$La$_{0.75}$Ti$_3$O$_{12}$ thin films. *Eur. Phys. J. B*, 38, 3, 431-436

[42] Hu, Z. G.; Strassburg, M.; Dietz, N.; Perera, A. G. U.; Asghar, A. & Ferguson, I. T. (2005). Composition dependence of the infrared dielectric functions in Si-doped hexagonal Al$_x$Ga$_{1-x}$N films on c-plane sapphire substrates. *Phys. Rev. B*, 72, 24, 245326(1-10)

[43] Hu, Z. G.; Weerasekara, A. B.; Dietz, N.; Perera, A. G. U.; Strassburg, M.; Kane, M. H.; Asghar, A. & Ferguson, I. T. (2007). Infrared optical anisotropy of diluted magnetic Ga$_{1-x}$Mn$_x$N/c-sapphire epilayers grown with a GaN buffer layer by metalorganic chemical vapor deposition. *Phys. Rev. B*, 75, 20, 205320(1-8)

[44] Djurišić, A. B.; Chan, Y. & Li, E. H. *Mater. Sci. Eng. R*, (2002). Progress in the room-temperature optical functions of semiconductors. 38, 6, 237-293

[45] Chen, C.; An, I. & Collins, R. W. (2003). Multichannel mueller matrix ellipsometry for simultaneous real-time measurement of bulk isotropic and surface anisotropic complex dielectric functions of semiconductors. *Phys. Rev. Lett.*, 90, 21, 217402(1-4)

[46] Kasic, A.; Schubert, M.; Einfeldt, S.; Hommel, D. & Tiwald, T. E. (2000). Free-carrier and phonon properties of n- and p-type hexagonal GaN films measured by infrared

ellipsometry. *Phys. Rev. B.*, 62, 11, 7365-7377

[47] Hu, Z. G.; Meng, X. J.; Huang, Z. M.; Wang, G. S.; Zhao, Q. & Chu, J. H. (2003). Thickness dependence of infrared optical properties of $LaNiO_3$ thin films prepared on platinized silicon substrates. *Jpn. J. Appl. Phys.*, 42, 11, 7045-7049

[48] Hu, Z. G.; Li, Y. W.; Zhu, M.; Zhu, Z. Q. & Chu, J. H. (2008). Structure and optical properties of ferroelectric $PbZr_{0.40}Ti_{0.60}O_3$ films grown on $LaNiO_3$-coated platinized silicon determined by infrared spectroscopic ellipsometry. *J. Phys. Chem. C*, 112, 26, 9737-9743

[49] Hu, Z. G.; Huang, Z. M. & Chu, J. H. (2005). *Trends in Semiconductor Research*, edited by Thomas B. Elliot, Chapter 5, page: 111-136, ISBN: 1-59454-414-X, Nova Science Publishers, Inc. NY

[50] Azzam, R. M. A. & Bashara, N. M. (1999). *Ellipsometry and Polarized Light*, Chapter 3, Page: 153-267, ISBN: 0-444-87016-4, North-Holland, Amsterdam

[51] Li, W. W.; Hu, Z. G.; Li, Y. W.; Zhu, M.; Zhu, Z. Q. & Chu, J. H. (2010). Growth, microstructure, and infrared-ultraviolet optical conductivity of $La_{0.5}Sr_{0.5}CoO_3$ nanocrystalline films on silicon substrates by pulsed laser deposition. *ACS Appl. Mater. Interfaces*, 02, 3, 896-902

[52] Adachi, S. (1987). Model dielectric constants of GaP, GaAs, GaSb, InP, InAs, and InSb. *Phys. Rev. B*, 35, 14, 7454-7463

[53] Hu, Z. G.; Wang, G. S.; Huang, Z. M.; Meng, X. J.; Shi, F. W. & Chu, J. H. (2003). Investigations of the optical properties of $Ba_{0.9}Sr_{0.1}TiO_3$ ferroelectric thin films by spectroscopic ellipsometry. *Jpn. J. Appl. Phys.*, 42, 3, 1400-1404

[54] Hu, Z. G.; Li, Y. W.; Zhu, M.; Zhu, Z. Q. & Chu, J. H. (2008). Composition dependence of dielectric function in ferroelectric $BaCo_xTi_{1-x}O_3$ films grown on quartz substrates by transmittance spectra. *Appl. Phys. Lett.*, 92, 08, 081904(1-3)

[55] Hu, Z. G.; Li, W. W.; Wu, J. D.; Sun, J.; Shu, Q. W.; Zhong, X. X.; Zhu, Z. Q. & Chu, J. H. (2008). Optical properties of pulsed laser deposited rutile titanium dioxide films on quartz substrates determined by Raman scattering and transmittance spectra. *Appl. Phys. Lett.*, 93, 18, 181910(1-3)

[56] Li, W. W.; Hu, Z. G.; Wu, J. D.; Sun, J.; Zhu, M.; Zhu, Z. Q. & Chu, J. H. (2009). Concentration dependence of optical properties in arsenic-doped ZnO nanocrystalline films grown on silicon (100) substrates by pulsed laser deposition. *J. Phys. Chem. C*, 113, 42, 18347-18352

[57] Kim, T. J.; Yoon, J. J.; Hwang, S. Y.; Aspnes, D. E.; Kim, Y. D.; Kim, H. J.; Chang, Y. C. & Song, J. D. (2009). Interband transitions of $InAs_xSb_{1-x}$ alloy films. *Appl. Phys. Lett.*, 95, 11, 111902(1-3)

[58] Yu, W. L.; Li, W. W.; Wu, J. D.; Sun, J.; Zhu, J. J.; Zhu, M.; Hu, Z. G. & Chu, J. H. (2010). Far-infrared-ultraviolet dielectric function, lattice vibration, and photoluminescence properties of diluted magnetic semiconductor $Sn_{1-x}Mn_xO_2/c$-sapphire nanocrystalline films. *J. Phys. Chem. C*, 114, 18, 8593-8600

[59] Qazilbash, M. M.; Schafgans, A. A.; Burch, K. S.; Yun, S. J.; Chae, B. G.; Kim, B. J.; Kim, H. T. & Basov, D. N. (2008). Electrodynamics of the vanadium oxides VO_2 and V_2O_3. *Phys. Rev. B*, 77, 11, 115121(1-10)

[60] Hu, Z. G.; Wang, G. S.; Huang, Z. M.; Meng, X. J. & Chu, J. H. (2002). Infrared optical properties of $Bi_{3.25}La_{0.75}Ti_3O_{12}$ ferroelectric thin films using spectroscopic ellipsometry. *J. Phys. D: Appl. Phys.*, 35, 24, 3221-3224

[61] Hu, Z. G.; Wang, G. S.; Huang, Z. M.; Meng, X. J. & Chu, J. H. (2003). Investigations

on the infrared optical properties of $BaTiO_3$ ferroelectric thin films by spectroscopic ellipsometry. *Semicond. Sci. Technol.*, 18, 6, 449-453

[62] Palik, E. D. (1985). *Handbook of Optical Constants of Solids*, Page: 341, Academic, Orlando. FL

[63] Hu, Z. G.; Li, Y. W.; Yue, F. Y.; Zhu, Z. Q. & Chu, J. H. (2007). Temperature dependence of optical band gap in ferroelectric $Bi_{3.25}La_{0.75}Ti_3O_{12}$ films determined by ultraviolet transmittance measurements. *Appl. Phys. Lett.*, 91, 22, 221903(1-3)

[64] Subbarao, E. C. (1961). Ferroelectricity in $Bi_4Ti_3O_{12}$ and its solid solutions. *Phys. Rev.*, 122, 3, 804-807

[65] Tsunekawa, S.; Ito, S.; Kawazoe, Y. & Wang, J. T. (2003). Critical size of the phase transition from cubic to tetragonal in pure zirconia nanoparticles. *Nano Lett.*, 3, 7, 871-875

[66] Cross, L. E. & Pohanka, R. C. (1968). A thermodynamic analysis of ferroelectricity in bismuth titanate. *J. Appl. Phys.*, 39, 8, 3992-3995

[67] Bennett, J. W.; Grinberg, L. & Rappe, A. M. (2008). New highly polar semiconductor ferroelectrics through d^8 cation-O vacancy substitution into $PbTiO_3$: A theoretical study. *J. Am. Chem. Soc.*, 130, 51, 17409-17412

[68] Arslan, M.; Duymus, H. & Yakuphanoglu, F. (2006). Optical properties of the poly(N-benzylaniline) thin film. *J. Phys. Chem. B*, 110, 1, 276-280

[69] Hu, Z. G.; Li, Y. W.; Zhu, M.; Yue, F. Y.; Zhu, Z. Q. & Chu, J. H. (2008). Growth and ellipsometric characterizations of highly (111) oriented $Bi_2Ti_2O_7$ films on platinized silicon by metal organic decomposition method. *J. Vac. Sci. Technol. A*, 26, 5, 1287-1292

[70] Myhre, C. E. L.; Christensen, D. H.; Nicolaisen, F. M. & Nielsen, C. J. (2003). Spectroscopic study of aqueous H_2SO_4 at different temperatures and compositions: Variations in dissociation and optical Properties. *J. Phys. Chem. A*, 107, 12, 1979-1991

[71] Hu, Z. G.; Li, Y. W.; Zhu, M.; Zhu, Z. Q.; & Chu, J. H. (2008). Microstructural and optical investigations of sol-gel derived ferroelectric $BaTiO_3$ nanocrystalline films determined by spectroscopic ellipsometry. *Phys. Lett. A*, 372, 24, 4521-4526

[72] Alivisatos, A. P. (1996). Semiconductor clusters, nanocrystals, and quantum dots. *Science*, 271, 5251, 933-937

[73] Frey, M. H. & Payne, D. A. (1996). Grain-size effect on structure and phase transformations for barium titanate. *Phys. Rev. B*, 54, 5, 3158-3168

[74] Bozovic, I.; Kim, J. H.; Harris, J. S.; Eom, C. B.; Phillips, J. M. & Cheung, J. T. (1994). Reflectance and Raman spectra of metallic oxides, LaSrCoO and CaSrRuO: Resemblance to superconducting cuprates. *Phys. Rev. Lett.*, 73, 10, 1436-1439

[75] Rusydi, A.; Rauer, R.; Neuber, G.; Bastjan, M.; Mahns, I.; Müller, S.; Saichu, P.; Schulz, B.; Singer, S. G.; Lichtenstein, A. I.; Qi, D.; Gao, X.; Yu, X.; Wee, A. T. S.; Stryganyuk, G.; Dörr, K.; Sawatzky, G. A.; Cooper, S. L. & Rübhausen, M. (2008). Metal-insulator transition in manganites: Changes in optical conductivity up to 22 eV. *Phys. Rev. B*, 78, 12, 125110(1-5)

[76] Barman, S. R.; Chainani, A. & Sarma, D. D. (1994). Covalency-driven unusual metal-insulator transition in nickelates. *Phys. Rev. B*, 49, 12, 8475-8478

[77] Dobin, A. Yu.; Nikolaev, K. R.; Krivorotov, I. N.; Wentzcovitch, R. M.; Dahlberg, E. D. & Goldman, A. M. (2003). Electronic and crystal structure of fully strained $LaNiO_3$ films. *Phys. Rev. B*, 68, 11, 113408(1-4)

[78] Bao, D. H.; Yao, X.; Wakiya, N.; Shinozaki, K. & Mizutani, N. (2001). Band-gap energies of sol-gel-derived $SrTiO_3$ thin films. *Appl. Phys. Lett.*, 79, 23, 3767-3769

[79] Majumder, S. B.; Jain, M. & Katiyar, R. S. (2002). Investigations on the optical properties of sol-gel derived lanthanum doped lead titanate thin films. *Thin Solid Films*, 402, 1-2, 90-98

[80] Franke, E.; Trimble, C. L.; Devries, M. J.; Woollam, J. A.; Schubert, M. & Frost, F. (2000). Dielectric function of amorphous tantalum oxide from the far infrared to the deep ultraviolet spectral region measured by spectroscopic ellipsometry. *J. Appl. Phys.*, 88, 9, 5166-5174
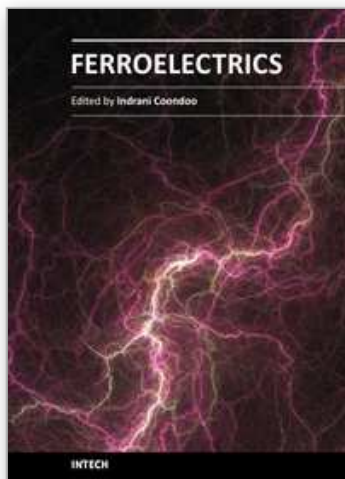
Ferroelectrics

Edited by Dr Indrani Coondoo

ISBN 978-953-307-439-9

Hard cover, 450 pages

Publisher InTech

Published online 14, December, 2010

Published in print edition December, 2010

Ferroelectric materials exhibit a wide spectrum of functional properties, including switchable polarization, piezoelectricity, high non-linear optical activity, pyroelectricity, and non-linear dielectric behaviour. These properties are crucial for application in electronic devices such as sensors, microactuators, infrared detectors, microwave phase filters and, non-volatile memories. This unique combination of properties of ferroelectric materials has attracted researchers and engineers for a long time. This book reviews a wide range of diverse topics related to the phenomenon of ferroelectricity (in the bulk as well as thin film form) and provides a forum for scientists, engineers, and students working in this field. The present book containing 24 chapters is a result of contributions of experts from international scientific community working in different aspects of ferroelectricity related to experimental and theoretical work aimed at the understanding of ferroelectricity and their utilization in devices. It provides an up-to-date insightful coverage to the recent advances in the synthesis, characterization, functional properties and potential device applications in specialized areas.

How to reference

In order to correctly reference this scholarly work, feel free to copy and paste the following:

Zhigao Hu, Yawei Li, Wenwu Li, Jiajun Zhu, Min Zhu, Ziqiang Zhu and Junhao Chu (2010). Optical Properties and Electronic Band Structures of Perovskite-Type Ferroelectric and Conductive Metallic Oxide Films, Ferroelectrics, Dr Indrani Coondoo (Ed.), ISBN: 978-953-307-439-9, InTech, Available from: http://www.intechopen.com/books/ferroelectrics/optical-properties-and-electronic-band-structures-of-perovskite-type-ferroelectric-and-conductive-me

InTech Europe

University Campus STeP Ri

Slavka Krautzeka 83/A

51000 Rijeka, Croatia

Phone: +385 (51) 770 447

Fax: +385 (51) 686 166

www.intechopen.com

InTech China

Unit 405, Office Block, Hotel Equatorial Shanghai

No.65, Yan An Road (West), Shanghai, 200040, China

中国上海市延安西路65号上海国际贵都大饭店办公楼405单元

Phone: +86-21-62489820

Fax: +86-21-62489821